

Armchair edge states in shear-strained graphene: Magnetic properties and quantum valley Hall edge states

Ruigang Li,¹ Pei-Hao Fu², Jun-Feng Liu^{1,*} and Jun Wang^{3,†}

¹*School of Physics and Materials Science, Guangzhou University, Guangzhou 510006, China*

²*Science, Mathematics and Technology, Singapore University of Technology and Design, Singapore 487372, Singapore*

³*Department of Physics, Southeast University, Nanjing 210096, China*



(Received 22 August 2023; revised 20 November 2023; accepted 12 December 2023; published 3 January 2024)

Typically, edge states in graphene are known to exist solely along zigzag edges. However, in this paper, we present a theoretical discovery of edge states along armchair edges in graphene under shear strain. This phenomenon arises from shear strain causing a separation between two inequivalent Dirac cones in the Brillouin zone (BZ) along the zigzag direction. Consequently, these armchair edge states appear as flat bands, connecting the two Dirac points at the two edges of armchair graphene nanoribbons (AGNRs). The length of these flat bands in the BZ and the penetration depth of the edge states are directly and inversely proportional to the strain, respectively. In monolayer AGNRs, possible magnetic configurations of flat bands resulting from electron-electron interactions are investigated. The edge-to-edge antiferromagnet (AFM) ground state is found in neutral AGNRs, while the AFM to ferromagnet (FM) transition can occur and be controlled by the strain in low-doped AGNRs. In gapped bilayer AGNRs, the armchair edge states evolve into quantum valley Hall edge states (QVHESs), which significantly improves the conductivity of QVHESs at realistic imperfect sample edges. These armchair edge states present a promising and tunable platform for exploring topological edge states in graphene.

DOI: [10.1103/PhysRevB.109.045403](https://doi.org/10.1103/PhysRevB.109.045403)

I. INTRODUCTION

Graphene is an ideal platform to engineer ample topological bulk phases and topological edge states (TESs) [1,2]. Even in pristine graphene, two valleys with opposite Berry phases are connected by the zero-energy flat band along zigzag edges. These well-known zigzag edge states (ZESs) in graphene have a topological origin, are quite robust against weak perturbations, and have been experimentally verified [3–8]. The magnetic structures of zigzag-edge flat bands have been widely studied based on the electron-electron interaction [9–17]. The edge-to-edge antiferromagnet (AFM) ground state was found in neutral narrow zigzag graphene nanoribbons (ZGNRs). The phase diagrams in finite-doped ZGNRs were also reported and the magnetic phase transition was found [18,19]. This edge magnetism of ZESs is particularly promising for spintronic applications [13,20–22]. However, the edge magnetism is sensitive to edge defects due to the short penetration depth of ZESs [23].

In bilayer graphene, these ZESs evolve into quantum valley Hall edge states (QVHESs) when a perpendicular electric field is applied to bilayer ZGNRs to open a bulk gap [24,25]. These QVHESs host great promise for low-dissipation transport channels and topological transistors or devices [26–29]. Unfortunately, the QVHESs are only found along zigzag edges and are fragile to edge defects.

Usually, these edge states in graphene are believed to occur solely along zigzag edges. In fact, the separation of two valleys is the key point to induce edge states in graphene nanoribbons. The bare armchair nanoribbons (AGNRs) do not host edge states due to the superposition of two valleys. But when the three nearest hopping energies satisfy the condition $t_1 < t_2 < t_3$ with t_2 , the hopping energy parallel to the armchair direction, the zero-energy armchair edge states (AESs) were predicted to exist [30]. In this paper, we apply a shear strain to AGNRs and predict the existence of these AESs, which is consistent with the hopping energy condition [30]. It is because the shear strain can separate two valleys along the zigzag direction of the reciprocal space of graphene [31–34] via the effective pseudovector potential [35,36]. The elastic deformation can be applied to the graphene lattice beyond 20% [37]. We further find more robust edge magnetizations of these AESs in monolayer AGNRs against edge defects due to the strain-tunable penetration depth of AESs. An AFM ground state is found in neutral AGNRs while the AFM to FM transition is found and controllable by the strain in low-doped AGNRs. In gapped bilayer AGNRs, the AESs also evolve into QVHESs, which significantly improves the conductivity of QVHESs at realistic imperfect sample edges.

II. AESS IN AGNRs UNDER SHEAR STRAIN

A shear-deformed monolayer AGNR (S-MAGNR) with width N is shown in Fig. 1(a). There are N A sites and N B sites in the supercell circled by the blue dot rectangle. The nearest-neighbor hopping energy $t = 3$ eV is taken as

*phjfliu@gzhu.edu.cn

†jwang@seu.edu.cn

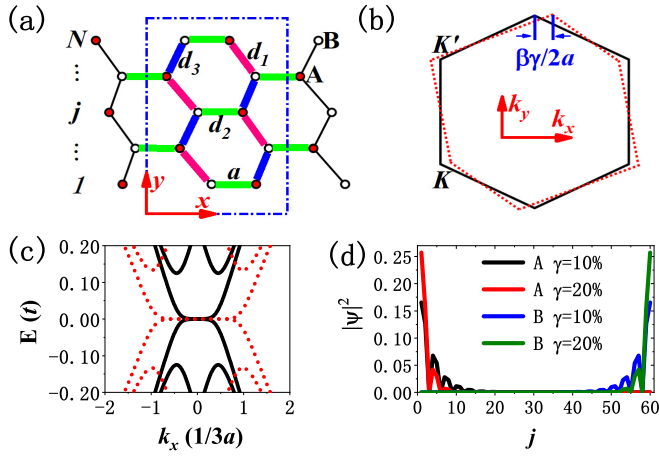


FIG. 1. (a) Schematic of the AGNR after shear deformation, with the strain applied along the armchair direction. (b) BZ of shear-deformed graphene. (c) The band structures of S-MAGNR with $N = 60$ and $\gamma = 10\%/20\%$ (black solid lines/red dot lines). (d) The corresponding wave function distributions of the flat bands at $k_x = 0$.

the unit of energy and the length of the C-C bond is $a = 1.42 \text{ \AA}$ before deformation. With the shear strain applied along the armchair direction, the lengths of deformed bonds are given as $d_\alpha = a\sqrt{1 + \epsilon_\alpha}$, with $\alpha = 1, 2, 3$ [37]. In detail, $\epsilon_1 = \sqrt{3}\gamma(\sqrt{3}\gamma - 2)/4$, $\epsilon_2 = 0$, $\epsilon_3 = \sqrt{3}\gamma(\sqrt{3}\gamma + 2)/4$ and γ is the shear strain parameter [34]. The hopping energies after deformation are given by $t_\alpha = t \exp[-\beta(d_\alpha/a - 1)]$, where $\beta = 3.37$ is the Grüneisen parameter [35].

The field operator at the j th row atoms can be defined as $\psi_j = (a_{j\sigma}, b_{j\sigma})^T$, where $a_{j\sigma}$ ($b_{j\sigma}$) is the annihilation operator at the j th row A (B) site with spin $\sigma = \uparrow, \downarrow$. Then we can obtain the spin-resolved tight-binding Hamiltonian of S-MAGNR

$$H_\sigma^S = \sum_{j=1}^N \psi_{j\sigma}^\dagger I_j \psi_{j\sigma} + \left(\sum_{j=1}^{N-1} \psi_{j\sigma}^\dagger O_j \psi_{j+1,\sigma} + \text{H.c.} \right), \quad (1)$$

where

$$I_j = \begin{pmatrix} 0 & t_2 e^{ik_x a} \\ t_2 e^{-ik_x a} & 0 \end{pmatrix}, \quad O_j = \begin{pmatrix} 0 & t_3 e^{-ik_x a/2} \\ t_1 e^{ik_x a/2} & 0 \end{pmatrix}.$$

I_j and O_j denote the intrarow and interrow hopping, respectively.

By numerically diagonalizing the Hamiltonian, two degenerate AESs appear as two flat bands for S-MAGNRs with $N = 60$ and $\gamma = 10\%$ and 20% , as shown in Fig. 1(c). The corresponding wave function distributions at $k_x = 0$ are shown in Fig. 1(d) for various strain strength. The flat bands originate from the shear strain induced separation of two valleys that are originally superposed at $k_x = 0$. Along the k_x direction, the separation between two valleys would be $L_F \approx \beta\gamma/a$, sketched in Fig. 1(b) [34]. We also define L_F as the length of two flat bands in the momentum space, which is approved by the results in Fig. 1(c). Note that L_F is proportional to the shear strain strength γ .

The wave functions of AESs can be solved analytically. Consider a semi-infinite graphene with an armchair edge at

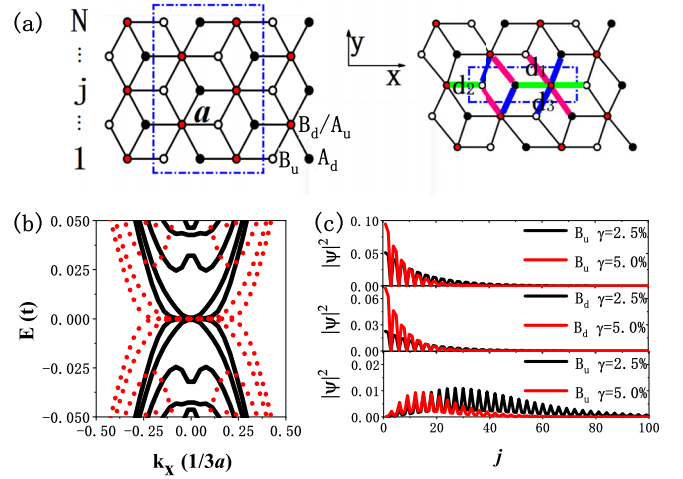


FIG. 2. (a) Schematic of the bilayer armchair graphene nanoribbon (left) before and (right) after shear deformation, with the strain applied along the armchair direction. (b) The band structures of S-MAGNR with $N = 200$ and $\gamma = 2\%/5\%$ (black solid lines/red dot lines) and (c) the corresponding wave function amplitudes of the edge states at $k_x = 0$. The wave functions of the edge states in the upper, middle, and bottom panels are given by formulas (7), (5), and (9) in the Supplemental Material [38], respectively. The wave function at A sites $\alpha_{d/u} = 0$ [38].

$j = 1$, the Harper equation reads

$$\begin{aligned} E\alpha_j &= -t_1 e^{ik_x a/2} \beta_{j+1} - t_2 e^{-ik_x a} \beta_j - t_3 e^{ik_x a/2} \beta_{j-1}, \\ E\beta_j &= -t_1 e^{-ik_x a/2} \alpha_{j-1} - t_2 e^{ik_x a} \alpha_j - t_3 e^{-ik_x a/2} \alpha_{j+1}, \end{aligned} \quad (2)$$

where α_j (β_j) is the wave function of the j th row A (B) site. At the edge with $j = 1$, the equation becomes

$$\begin{aligned} E\alpha_1 &= -t_1 e^{ik_x a/2} \beta_2 - t_2 e^{-ik_x a} \beta_1, \\ E\beta_1 &= -t_2 e^{ik_x a} \alpha_1 - t_3 e^{-ik_x a/2} \alpha_2. \end{aligned} \quad (3)$$

At $k_x = 0$, without loss of generality, the wave function of zero energy flat bands can be found as

$$\alpha_j = 0, \quad \beta_j = \begin{cases} e^{-\lambda y_j/2} \beta_1, & j = 3n - 2 \\ -e^{-\lambda y_j/2} \beta_1, & j = 3n - 1 \\ 0, & j = 3n, \end{cases} \quad (4)$$

where $n \in \mathbb{N}^+$. $y_j = \sqrt{3}(j-1)a/2$ is the y coordinate of j th row atoms. $\lambda = \beta\gamma/a$ denotes the penetration coefficient of the wave function, which is only determined by the strain parameter γ . Away from $k_x = 0$, the wave functions become k_x dependent but still are restricted by the decay factor $e^{-\lambda y_j/2}$ at $E = 0$. Therefore, the penetration depth of edge states can be defined as $y_D = 1/\lambda = a/\beta\gamma$, which is inversely proportional to the shear strain strength. For $\gamma = 1\%$, the penetration depth would be $y_D \approx 30a$, which contains 35 rows of atoms.

Similarly, AESs can also emerge as flat bands in shear-deformed bilayer AGNR (S-BAGNR) [38]. The BAGNR is shown in Fig. 2(a). There are $N A_{d/u}$ atoms (black/red dot) and $N B_{d/u}$ atoms (red/white dot) in the supercell, which is circled by the blue dot rectangle in Fig. 2(a). $A_{d/u}$ ($B_{d/u}$) denotes the A atoms (B atoms) of the bottom/upper layer. The nearest-neighbor hopping energy t and the interlayer hopping

energy between B_d and A_u atoms is $t' = 0.1t$. Note that the interlayer hopping energy remains the same with the shear strain applied.

The field operator at j th row atoms can be defined as $\Psi_j = [a_d(j), b_d(j), a_u(j), b_u(j)]^T$, where $a_d(j)$ [$b_d(j)$, $a_u(j)$, $b_u(j)$] denotes the annihilation operator at $A_d(j)$ atom [$B_d(j)$, $A_u(j)$, $B_u(j)$] atom. Then we can obtain the tight-binding Hamiltonian of S-BAGNR

$$H^B = \sum_{j=1}^N \Psi_j^\dagger I_j^B \Psi_j + \left(\sum_{j=1}^{N-1} \Psi_j^\dagger O_j^B \Psi_{j+1} + \text{H.c.} \right), \quad (5)$$

where

$$I_j^B = \begin{pmatrix} -V_0 & t_2 e^{ik_x a} & 0 & 0 \\ t_2 e^{-ik_x a} & -V_0 & t' & 0 \\ 0 & t' & V_0 & t_2 e^{ik_x a} \\ 0 & 0 & t_2 e^{-ik_x a} & V_0 \end{pmatrix},$$

$$O_j^B = \begin{pmatrix} 0 & t_3 e^{-ik_x a/2} & 0 & 0 \\ t_1 e^{ik_x a/2} & 0 & 0 & 0 \\ 0 & 0 & 0 & t_3 e^{-ik_x a/2} \\ 0 & 0 & t_1 e^{ik_x a/2} & 0 \end{pmatrix}.$$

I_j^B and O_j^B denote the intrarow and interrow hoppings, respectively. V_0 in I_j^B is introduced by the perpendicular electric field. When $V_0 = 0$, the AESs appear as flat bands and the corresponding wave function amplitudes at $k_x = 0$ are obtained and shown in Figs. 2(b) and 2(c), respectively. The length of flat band in momentum space is $L_F^B \approx \beta\gamma/a$ [38], which is consistent with the results in Fig. 2(b). The flat band is constructed within $|k_x| < \beta\gamma/2a$, determined by the strain.

AESs emerge in all metallic S-MAGNRs and S-BAGNRs with $N = 3p - 1$ and $p \in \mathbb{N}^+$. For S-MAGNRs and S-BAGNRs with $N \neq 3p - 1$, AESs only emerge after the strain is strong enough to close the finite-size-induced gap. The details are presented in the Supplemental Material [38].

III. SPONTANEOUS FERROMAGNETISM OF AES

Similar to ZESs, the AESs can induce spontaneous magnetic order in S-MAGNRs by considering the electron-electron interaction within the Hubbard model. The Hamiltonian can be written as $H = \sum_{\sigma} [H_{\sigma}^S + H_{\sigma}^U]$. $H_{\sigma}^U = U \sum_j [\langle n_{j\bar{\sigma}} \rangle - 1/2] n_{j\sigma}$ [39] represents the on-site repulsive interaction, where $n_{j\sigma} = \psi_{j\sigma}^\dagger \psi_{j\sigma}$ is the density operator of electron with spin σ at the j th row atoms and $\langle n_{j\sigma} \rangle$ denotes the corresponding expectation value. $\bar{\sigma}$ denote the opposite spin to σ . Without loss of generality, $U = 3.24$ eV [9] stands for the magnitude of the on-site Coulomb repulsion in this paper.

By setting an initial magnetic configuration, the band structure and the magnetic moment $\langle M \rangle$ at A_j atom (B_j atom), i.e., $\langle M_{A_j} \rangle = \langle a_{j\uparrow}^\dagger a_{j\uparrow} \rangle - \langle a_{j\downarrow}^\dagger a_{j\downarrow} \rangle$ ($\langle M_{B_j} \rangle = \langle b_{j\uparrow}^\dagger b_{j\uparrow} \rangle - \langle b_{j\downarrow}^\dagger b_{j\downarrow} \rangle$), can be obtained by self-consistent iterations, in units of μ_B . Both edge-to-edge AFM and FM configurations are stable. For simplicity, we consider only the situation of zero temperature. Note that this spontaneous edge ferromagnetism of AESs should be more robust against edge defects than that of ZESs. This is because the penetration depth of AESs is much larger than that of ZESs and strain tunable, while ZESs are mainly localized at the outermost edge atoms.

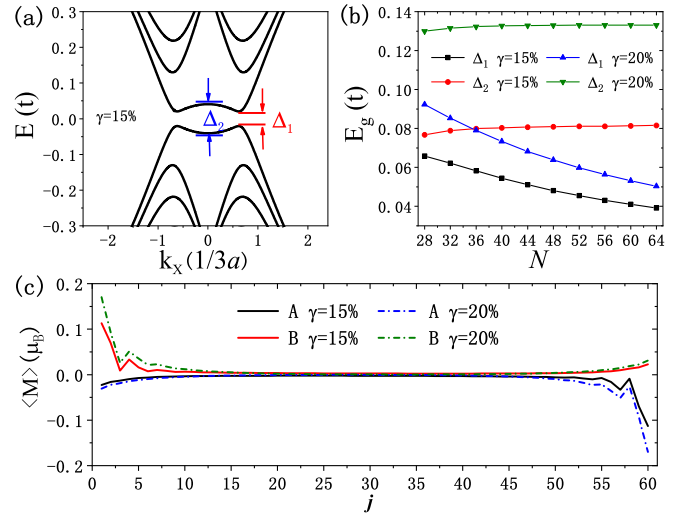


FIG. 3. (a) The band structure of edge-to-edge antiferromagnetic S-MAGNR with $N = 60$ and $\gamma = 15\%$. (b) The band gaps as functions of nanoribbon width N with $\gamma = 15\%/20\%$. (c) The local magnetic moment of $N = 60$ S-MAGNR with $\gamma = 15\%/20\%$.

According to Lieb's theorem [9], the total magnetism of the ground state is zero in a half-filled bipolar lattice. The results of the AFM ground state for half-filling S-MAGNRs are shown in Fig. 3. The band structure is spin degenerate and the on-site repulsive interaction opens a band gap Δ_1 separating the valence and conduction band. In the original flat-band region $|k_x| < \beta\gamma/2a$, the gap changes with k_x , with the minimal value Δ_1 at around $k_x = \pm\beta\gamma/2a$ and the maximal value Δ_2 at $k_x = 0$, as shown in Fig. 3(a). As shown in Fig. 3(b), Δ_1 decreases with increasing width and decreasing strain. By contrast, Δ_2 barely changes with nanoribbon width, but is sensitive to the strain. The local magnetizations of $N = 60$ S-MAGNRs exhibit AFM edge magnetizations as shown in Fig. 3(c). The maximal on-site magnetic moment increases with increasing strain. When $\gamma = 15\%$ (20%), the maximal magnetic moment $\langle M_{A/B} \rangle$ is around $0.11 \mu_B$ ($0.17 \mu_B$).

The edge-to-edge FM configuration can also be obtained, but with a slightly higher energy than the AFM one, for the neutral S-MAGNR. The energy difference per carbon atom between the AFM and FM orders decreases with increasing width N . Figure 4(a) shows the spin-split band structure of $N = 60$ S-MAGNRs. The corresponding local magnetizations are shown in Fig. 4(b).

In the case of finite doping, the FM order can also be the ground state. By doping n_D electrons per supercell to the neutral S-MAGNR, the transition between AFM and FM orders becomes possible. In the case of low-doping, the band structures for both the AFM and FM orders barely change. But the total energy of electrons is sensitive to the doping. The total energy for the FM/AFM order reads

$$E_{\text{tot}}^{\text{FM/AFM}} = \frac{1}{N_{k_x}} \sum_{m, k_x, \sigma}^{\text{Occ}} \varepsilon_{m, k_x, \sigma}, \quad (6)$$

where $N_{k_x} = 2000$ is taken as the number of k_x points in the BZ without loss of generality. $\varepsilon_{m, k_x, \sigma}$ denotes the eigenenergy of k_x state at the m th occupied band, with spin σ . The

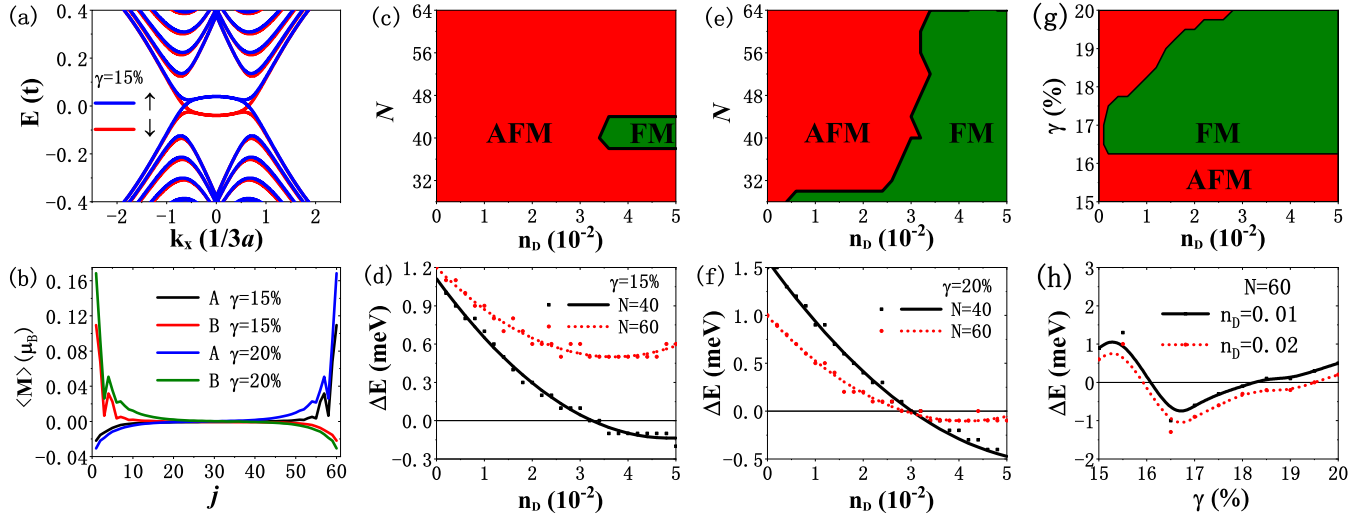


FIG. 4. (a) The band structure of edge-to-edge ferromagnetic S-MAGNR with $N = 60$ and $\gamma = 15\%$. (b) The local magnetic moment of $N = 60$ S-MAGNR with $\gamma = 15\%$ and 20% . (c), (e) The phase diagram of the magnetic order as functions of n_D and N with (c) $\gamma = 15\%$ and (e) 20% . (d), (f) The corresponding energy difference between the FM and AFM orders is the function of n_D with $N = 40$ and 60 . (g) The phase diagram as functions of γ and n_D with $N = 60$. (h) The corresponding energy difference as the function of γ with fixed $n_D = 10^{-2}$ and 2×10^{-2} .

energy difference between the FM and AFM orders, i.e., $\Delta E = E_{\text{tot}}^{\text{FM}} - E_{\text{tot}}^{\text{AFM}}$, determines the ground state. The doped electrons will occupy the states at the bottom of the conduction band above the neutral point. The AFM order is gapped while the FM order remains gapless. Therefore, the doped electrons in the AFM order will increase more energies than those in the FM order. As a result, $\Delta E > 0$ at $n_D = 0$ may turn into $\Delta E < 0$ for finite electron doping, which leads to the AFM to FM transition.

The phase diagrams of the magnetic order as functions of n_D and N are shown in Figs. 4(c) and 4(e). It is seen that the doping-induced AFM to FM transition only occurs in a narrow width range for $\gamma = 15\%$, but occurs in a much wider width range for $\gamma = 20\%$. Figures 4(d) and 4(f) show the corresponding energy difference between the FM and AFM orders as the function of n_D with $N = 40$ and 60 . Naturally, at fixed width N and doping n_D , the AFM to FM transition can be controlled by the applied strain, which can be seen in the phase diagram shown in Figs. 4(g) and 4(h). Interestingly, the AFM-FM-AFM transition can also be realized with increasing strain for suitable width and doping.

IV. QVHES IN GAPPED BILAYER AGNR

In gapped bilayer graphene under a perpendicular electric field, QVHESs across the gap can only exist along zigzag edges, which makes QVHESs very fragile to edge defects. As we know, the edge states vanish in gapped bilayer graphene with armchair termination [26,40,41]. Similar to ZESSs, AESs also evolve into QVHESs in gapped bilayer graphene. In S-BAGNRs, AESs can emerge as fourfold-degenerate flat bands as shown in the Supplemental Material [38]. By applying a perpendicular electric field, S-BAGNRs open a gap and two AESs evolve into QVHESs and cross the gap, as shown in Fig. 5(c). The corresponding wave function distributions of a QVHES are shown in Figs. 5(d) and 5(e).

To demonstrate the enhancement of the conductivity of QVHESs by AESs at realistic imperfect sample edges, we compare the conductances of QVHESs at zigzag and armchair

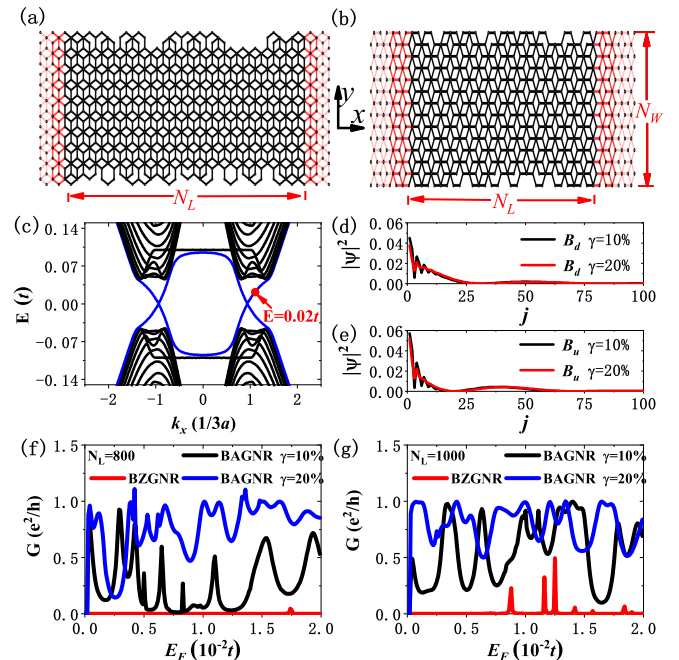


FIG. 5. (a), (b) Schematics of two junctions based on QVHESs at (a) zigzag and (b) armchair edges in gapped bilayer graphene ribbons. (c) The band structure of S-BAGNR with $N_W = 200$, $\gamma = 20\%$ and a perpendicular electric field $V_0 = 0.1t$. (d), (e) The wave-function distributions of the rightmost state at $E = 0.02t$ of S-BAGNR, with the applied strain $\gamma = 10\%$ and 20% . (f), (g) The conductances of two junctions shown in (a) and (b) with $N_W = 200$, $V_0 = 0.1t$, (f) $N_L = 800$ and (g) $N_L = 1000$. For S-BAGNRs, $\gamma = 10\%$ and 20% . E_F denotes the Fermi energy of the junction.

edges with edge defects. Without loss of generality, we consider two junctions with defects shown in Figs. 5(a) and 5(b). In both junctions, the leads are heavily doped. The bulk states of scattering regions are gapped by a perpendicular electric field (modeled by the on-site potential $-V_0$ and V_0 of the bottom and upper layer of bilayer graphene ribbons, respectively). For bilayer zigzag graphene nanoribbon (BZGNR) in Fig. 5(a), no strain is applied. For S-BAGNR in Fig. 5(b), a shear strain with $\gamma = 10\%$ and 20% is applied.

The conductances of two junctions are compared as shown in Figs. 5(f) and 5(g) with $N_L = 800$ and $N_L = 1000$, respectively. The calculation is carried out by the use of Kwant [42]. It is seen that the conductance of QVHESs at zigzag edges with defects is nearly zero. The QVHESs are almost completely reflected by the edge defects. Even so, the tunneling between broken QVHESs can still occur at edge defects in the device region, leading to resonance conductance thin peaks [shown in Fig. 5(g)]. By contrast, the conductance of QVHESs at armchair edges with defects reaches up to e^2/h for $\gamma = 20\%$. It implies that the QVHESs are much less reflected by the edge defects. The conductance difference can be understood roughly as follows. At armchair edges, the defect always removes pairs of *A* and *B* sites. While at zigzag edges, the defect removes one more *A* or *B* site. Roughly speaking, the zigzag edge defects have a smaller size than armchair edge defects, and thus induce heavier intervalley backscattering of QVHESs. Therefore, AESs significantly improve the conductivity of QVHESs at realistic imperfect sample edges. Besides, the AESs make the connectivity of QVHESs possible from zigzag edges to armchair edges (see the Supplemental

Material for details), which much extends the application ground of QVHESs.

V. CONCLUSION

We theoretically discovered AESs in graphene under shear strain. For both S-MAGNR and S-BAGNR, the length of the flat band (L_F) and the penetration depth of AES (y_D) were investigated. We found that the length of the flat band in the BZ and the penetration depth of AESs are directly and inversely proportional to the strain, respectively. Then we examined the spontaneous ferromagnetism of AESs in S-MAGNRs and found that the gaps and local magnetic moments in edge-to-edge AFM ground states for half filling can be tuned by the strain. Furthermore, strain controllable transitions between the edge-to-edge AFM and FM were found in low-doped S-MAGNRs. In gapped S-BAGNRs, the AESs evolve into QVHESs with relatively large penetration lengths, which significantly improves the conductivity of QVHESs at realistic imperfect sample edges.

ACKNOWLEDGMENTS

The work described in this paper is supported by the National Natural Science Foundation of China (Grants No. 12174077 and No. 12174051), the Science Foundation of Guangdong Province (Grant No. 2021A1515012363), the Guangdong Basic and Applied Basic Research Foundation (Grant No. 2022A1515110011), and the Bureau of Education of Guangzhou Municipality (Grant No. 202255464).

-
- [1] A. K. Geim and K. S. Novoselov, *Nat. Mater.* **6**, 183 (2007).
 [2] A. K. Geim, *Science* **324**, 1530 (2009).
 [3] T. T. Heikkilä, N. B. Kopnin, and G. E. Volovik, *JETP Lett.* **94**, 233 (2011).
 [4] G. E. Volovik, *J. Supercond. Novel Magn.* **26**, 2887 (2013).
 [5] D. Xiao, M. C. Chang, and Q. Niu, *Rev. Mod. Phys.* **82**, 1959 (2010).
 [6] R. S. K. Mong and V. Shivamoggi, *Phys. Rev. B* **83**, 125109 (2011).
 [7] M. Xiao, Z. Q. Zhang, and C. T. Chan, *Phys. Rev. X* **4**, 021017 (2014).
 [8] X. Huang, M. Xiao, Z. Q. Zhang, and C. T. Chan, *Phys. Rev. B* **90**, 075423 (2014).
 [9] E. H. Lieb, *Phys. Rev. Lett.* **62**, 1201 (1989).
 [10] M. Fujita, K. Wakabayashi, K. Nakada, and K. Kusakabe, *J. Phys. Soc. Jpn.* **65**, 1920 (1996).
 [11] S. Okada and A. Oshiyama, *Phys. Rev. Lett.* **87**, 146803 (2001).
 [12] H. Lee, Y.-W. Son, N. Park, S. Han, and J. Yu, *Phys. Rev. B* **72**, 174431 (2005).
 [13] Y.-W. Son, M. L. Cohen, and S. G. Louie, *Nature (London)* **444**, 347 (2006).
 [14] Y.-W. Son, M. L. Cohen, and S. G. Louie, *Phys. Rev. Lett.* **97**, 216803 (2006).
 [15] L. Pisani, J. A. Chan, B. Montanari, and N. M. Harrison, *Phys. Rev. B* **75**, 064418 (2007).
 [16] J. Fernández-Rossier, *Phys. Rev. B* **77**, 075430 (2008).
 [17] G. Z. Magda, X. Jin, I. Hagymási, P. Vancsó, Z. Osváth, P. Nemes-Incze, C. Hwang, L. P. Biró, and L. Tapasztó, *Nature (London)* **514**, 608-611 (2014).
 [18] J. Jung and A. H. MacDonald, *Phys. Rev. B* **79**, 235433 (2009).
 [19] K. Sawada, F. Ishii, M. Saito, S. Okada, and T. Kawai, *Nano Lett.* **9**, 269-272 (2009).
 [20] M. Wimmer, Í. Adagideli, S. Berber, D. Tománek, and K. Richter, *Phys. Rev. Lett.* **100**, 177207 (2008).
 [21] W. Y. Kim and K. S. Kim, *Nat. Nanotechnol.* **3**, 408 (2008).
 [22] F. Muñoz-Rojas, J. Fernández-Rossier, and J. J. Palacios, *Phys. Rev. Lett.* **102**, 136810 (2009).
 [23] B. Huang, F. Liu, J. Wu, Bing-Lin Gu, and W. Duan, *Phys. Rev. B* **77**, 153411 (2008).
 [24] E. V. Castro, N. M. R. Peres, J. M. B. Lopes dos Santos, A. H. Castro Neto, and F. Guinea, *Phys. Rev. Lett.* **100**, 026802 (2008).
 [25] F. Zhang, A. H. MacDonald, and E. J. Mele, *Proc. Natl. Acad. Sci. USA* **110**, 10546 (2013).
 [26] J. Feng, H. Tan, J.-F. Liu, and J. Wang, *Phys. Rev. Appl.* **19**, 024072 (2023).
 [27] J. Jung, F. Zhang, Z. Qiao, and A. H. MacDonald, *Phys. Rev. B* **84**, 075418 (2011).
 [28] Z. Qiao, J. Jung, Q. Niu, and A. H. MacDonald, *Nano Lett.* **11**, 3453 (2011).
 [29] J. Li, K. Wang, K. J. McFaul, Z. Zern, Y. Ren, K. Watanabe, T. Taniguchi, Z. Qiao, and J. Zhu, *Nat. Nanotechnol.* **11**, 1060 (2016).

- [30] G. Salerno, T. Ozawa, H. M. Price, and I. Carusotto, *Phys. Rev. B* **95**, 245418 (2017).
- [31] L. Yang and J. Han, *Phys. Rev. Lett.* **85**, 154 (2000).
- [32] Y. Li, X. Jiang, Z. Liu, and Z. Liu, *Nano Res.* **3**, 545 (2010).
- [33] C. Si, Z. Sun, and F. Liu, *Nanoscale* **8**, 3207 (2016).
- [34] R. Li, J.-F. Liu, and J. Wang, *Phys. Rev. Appl.* **19**, 024075 (2023).
- [35] V. M. Pereira and A. H. Castro Neto, *Phys. Rev. Lett.* **103**, 046801 (2009).
- [36] F. Zhai, X. Zhao, K. Chang, and H. Q. Xu, *Phys. Rev. B* **82**, 115442 (2010).
- [37] V. M. Pereira, A. H. Castro Neto, and N. M. R. Peres, *Phys. Rev. B* **80**, 045401 (2009).
- [38] See Supplemental Material at <http://link.aps.org/supplemental/10.1103/PhysRevB.109.045403> for information on armchair edge states in shear-deformed bilayer armchair graphene ribbons, the conditions of emergence of armchair edge states, and the connectivity of quantum valley Hall edge states between the zigzag edge and armchair edge.
- [39] B. Wunsch, T. Stauber, F. Sols, and F. Guinea, *Phys. Rev. Lett.* **101**, 036803 (2008).
- [40] J. Li, I. Martin, M. Büttiker, and A. F. Morpurgo, *Nat. Phys.* **7**, 38 (2011).
- [41] F. Zhang, J. Jung, G. A. Fiete, Q. Niu, and A. H. MacDonald, *Phys. Rev. Lett.* **106**, 156801 (2011).
- [42] C. W. Groth, M. Wimmer, A. R. Akhmerov, and X. Waintal, *New J. Phys.* **16**, 063065 (2014).